Chapter 3

Dual active bridge converter and its control

Ping Wang[1], **Zian Qin**[2], **Jing Yuan**[3] **and Frede Blaabjerg**[4]
[1]*Princeton University, Princeton, NJ, United States;* [2]*Delft University of Technology, Delft, Netherlands;* [3]*Aalborg University, Aalborg, Denmark;* [4]*AAU Energy, Aalborg University, Aalborg, Denmark*

3.1 Introduction

To mitigate the shortage of fossil-based energy resources, renewable energy sources (RESs) such as wind power and solar power have rapidly developed [1]. The power generation of these RESs, however, is usually irregular and intermittent. A large penetration level of RESs will therefore degrade the stability of AC power grids [2]. Energy storage systems (ESSs), which compensate for the mismatch between RES supply and load demand, can help improve grid stability and reliability [3]. On the other hand, there has been growing interest in DC distribution systems. Compared with conventional AC grids, DC distribution has the advantages of higher control flexibility, higher efficiency, the reduction of power conversion stages, and faster dynamic response [4–6]. It can also provide a natural interface with RESs and ESSs. These features enable DC distribution systems to be implemented in a wide range of applications including data centers, telecom systems, electric vehicles (EV), aircraft, and ships. The basic requirements for converters to interface ESSs with AC or DC power conversion systems are galvanic isolation and bidirectional power flow capability.

Fig. 3.1 shows the structure of a DC microgrid [7,8], which is mainly composed of (1) renewables (e.g., solar panel and wind turbine); (2) energy storage devices; (3) plug-in EVs; (4) smart home DC appliances; (5) utility grid connection; and (6) a solid-state transformer (SST)-based interface with different scales of microgrids [8]. Here, isolated bidirectional DC–DC (IBDC) converters are implemented as the interface of ESSs. When renewable power generation exceeds the demand load power, IBDC converters can store the extra power in energy storage devices for backup. During a power shortage, IBDC converters will discharge the energy storage devices to maintain the normal operation of important facilities. IBDC converters can

Control of Power Electronic Converters and Systems: Volume 4. https://doi.org/10.1016/B978-0-323-85622-5.00012-2

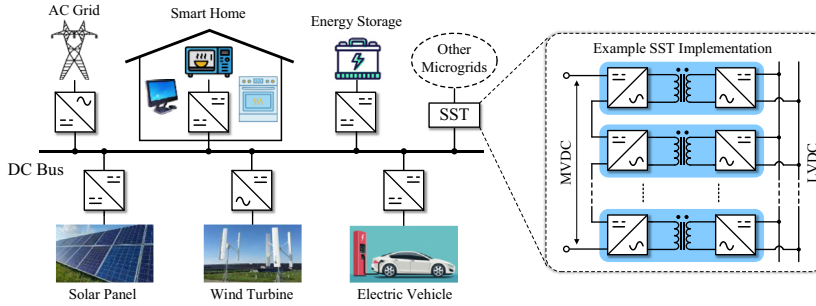

FIGURE 3.1 Structure of a DC microgrid composed of renewable energy sources, energy storage systems, plug-in electric vehicles, and smart home DC appliances. A solid-state transformer (SST) medium voltage DC-low voltage DC (MVDC-LVDC) implemented with stacked isolated bidirectional DC−DC submodules is shown as an example.

also be stacked as SSTs to interconnect different levels of DC grids [9], as shown in Fig. 3.1.

Various IBDC topologies have been explored, including resonant converters, dual-flyback converters, dual push-pull converters, and dual active bridge (DAB) converters. Among these converters, the DAB converter, which was first introduced in De Doncker et al. [10], is one of the most promising topologies. It delivers power through the leakage inductance of a high-frequency transformer and has the advantages of a simple and symmetric structure, zero-voltage switching (ZVS) capability, and a wide voltage conversion range. Research on DAB mainly focuses on the aspects of modulation schemes [11−21], modeling and control strategies [22−33], optimizations for ZVS range, current stress, and reactive power [13,34−44], and designs for specific applications such as an EV charger with vehicle-to-grid function [45], an uninterruptable power supply [46], and a differential power processing (DPP) converter for data center servers or series batteries [47,48]. Key research issues of DAB converters lie in trade-offs among the soft-switching range, voltage conversion range, reactive power, and component current stress.

Developed from the DAB, the multiactive-bridge (MAB) converter is gaining in popularity. It couples multiple active bridges with a single transformer and is able to handle multi-input-multioutput (MIMO) power flows. Unlike conventional MIMO converters that usually couple power flows through a DC voltage bus, the MAB converter delivers power by AC through the shared transformer. The AC coupling structure of the MAB converter reduces the component count, magnetic size, and power conversion stages, enabling high efficiency and a high power density converter design [49−52]. MAB has shown its potential in many applications including DPP converters [51], energy routers [52], and SSTs [53].

This chapter presents the operation principle and performance characterization of the DAB converter as well as its control. Various modulation methods are compared. Trade-offs among control complexity, the ZVS operation range, and component current stress are discussed. Large- and small-signal modeling approaches and different control strategies are also introduced. The modeling and control strategies are verified by practical DAB examples in PLECS simulations.

3.2 Operation principle and performance characterization of dual active bridge converter

3.2.1 Circuit topology and modulation schemes

Fig. 3.2 shows the circuit topology and equivalent model of a DAB converter. The DAB converter is composed of two active bridges linked by a power transfer inductor and a transformer. High step-up or step-down voltage conversion can be achieved by adjusting the transformer turns ratio. The power transfer inductor can be implemented using the leakage inductance of the transformer or with an additional series inductor. For convenience, we call it leakage inductance (L_k) in the following analysis. With a symmetric architecture, the DAB converter has the capability of natural bidirectional power flow and ZVS operation for all power switches.

Fig. 3.2B shows a simplified electrical model for a DAB converter. Two active bridges that generate different levels of voltages at two ports of the leakage inductance can be modeled as two AC voltage sources (v_p and v_s). Here, all parameters are converted into the primary side. Manipulating the switching of two active bridges will change the voltage across the leakage inductance and thereby influence the inductor current. As indicated in Fig. 3.2B, power transfer between two active bridges in a DAB converter is analogous to that of traditional AC power systems: the magnitude and direction of power flow can be controlled by modulating the phase shifts (PSs) between two AC voltage sources, and active power will flow from the leading voltage source to the lagging one in general.

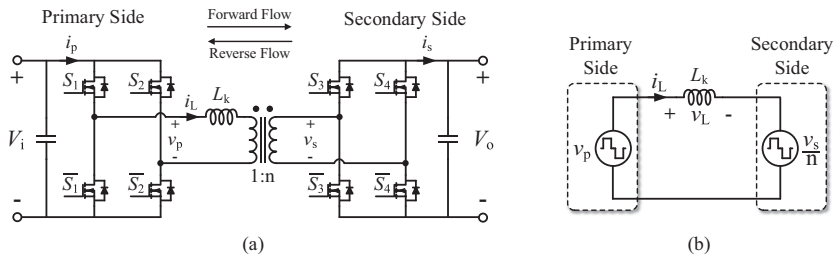

FIGURE 3.2 Dual active bridge (DAB) converter: (A) Circuit topology; (B) Simplified DAB model.

PS modulation is one of the most attractive modulation techniques for the DAB converter, and various PS modulation methods have been explored so far. Fig. 3.3 shows four typical PS modulation methods: single-PS (SPS) modulation [10,11], extended-PS (EPS) modulation [12−15], double-PS (DPS) modulation [16−18], and triple-PS (TPS) modulation [19−21].

(1) *SPS modulation method*: SPS modulation is the most basic and common modulation method, which came out directly with DAB topology when it was first introduced [10]. Fig. 3.3A depicts main operation waveforms of the SPS modulation. As shown in the figure, each active bridge generates a square-wave voltage with a fixed 50% duty ratio. Power flow is controlled by modulating the PS (denoted as φ) between the two square-wave voltages. Because there is only one controllable parameter, SPS modulation is simple and robust. DAB converters under SPS modulation have decent performance with low peak and root-mean-square (rms) current, ZVS-on capability of power switches, uniformly distributed power loss across all switches, and stable first-order dynamics, especially

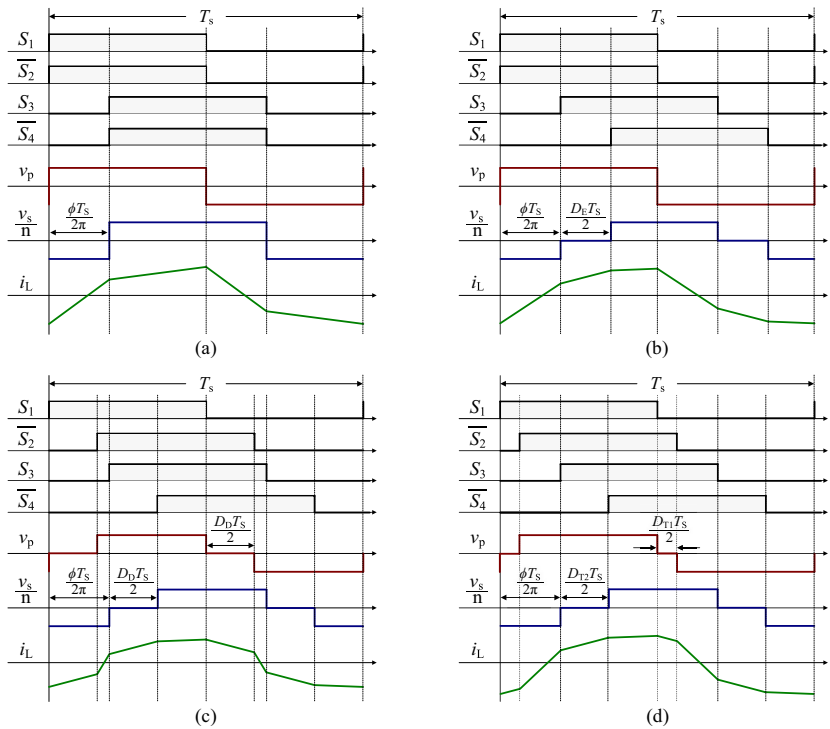

FIGURE 3.3 Typical modulation methods of dual active bridge converter in Fig. 3.2: (A) Single-phase shift (PS) modulation; (B) Extended-PS modulation ($D_E < \varphi/\pi$); (C) Double-PS modulation ($D_D < \varphi/\pi$); (D) Triple-PS modulation ($D_{T1} < D_{T2} < \varphi/\pi$).

when the input and output voltages are matched (i.e., $V_i = \frac{V_o}{n}$). However, when the input and output voltages are mismatched and deviate significantly from nominal values, the ZVS range will be greatly reduced and circulating power will become high, resulting in higher conduction loss and current stress on the power switches. To overcome this problem, alternative modulation methods such as EPS, DPS, and TPS modulation methods were proposed in the literature.

(2) *EPS modulation method:* EPS modulation is an modulation method improved from SPS. Besides the outer PS φ between two active bridges, EPS modulation has an inner PS in one of the active bridges. Denote the inner PS ratio as D_E. Fig. 3.3B shows main operation waveforms of EPS in an example case when D_E is at the secondary side and $D_E < \varphi/\pi$. Under EPS modulation, the active bridge without inner PS generates a symmetric square-wave voltage of 50% duty ratio, the same as in SPS modulation, but the active bridge with inner PS will generate a three-level voltage waveform. During the interval of zero-voltage level, the backflow power is zero [15]. Therefore, EPS modulation can effectively reduce the circulating power. In general, the outer PS of EPS modulation is used to control the power flow magnitude and direction, and the inner PS is used to decrease the circulating power and expand the ZVS range. Moreover, to achieve better efficiency of the DAB converter, the inner PS should be implemented at the high voltage side when the DAB shifts between the buck mode and boost mode.

(3) *DPS modulation method:* Like EPS modulation, DPS modulation has an outer PS and an inner PS as two controlled variables, but the inner PS will be implemented at both active bridges with the same PS ratio, denoted as D_D. Main waveforms of DPS modulation in an example case of $D_D < \varphi/\pi$ are plotted in Fig. 3.3C. As shown in the figure, both two active bridges generate a three-level voltage waveform. Compared with SPS modulation, DPS modulation can be used to expand the ZVS range and decrease the circulating power and current stress. Besides, because the two active bridges have identical inner PSs, their operation states remain the same when the voltage conversion mode or power flow direction changes. Thus, DPS modulation is relatively easier to implement than EPS modulation.

(4) *TPS modulation method:* Fig. 3.3D shows example operation waveforms of TPS modulation. Under TPS modulation, two active bridges are operated with an outer PS between them and inner PSs within both of them, so they will each generate a three-level voltage waveform, similar to that in DPS modulation. The difference is the inner PS ratios of the two active bridges can be different, which are denoted as D_{T1} and D_{T2}. Because TPS modulation has three controlled variables, it has more flexibility to shape the inductor current. Therefore, TPS modulation is

able to achieve the minimum circulating power, the minimum current stress, and the maximum ZVS range theoretically. The three controlled variables of TPS result in numerous modulation states, and there is no unified standard for implementing TPS. Research on TPS modulation mainly focuses on the optimized operation scheme to shift between different modulation states under different conditions for better performance [19–21, 38–44].

For any of the modulation methods shown in Fig. 3.3, each half-bridge is operated in the same way: the upper switch and lower switch are controlled by complementary pulse width modulation (PWM) signals with a fixed 50% duty ratio. The distinction lies in different PS schemes either between active bridges or within one active bridge. Among the four modulation methods, TPS modulation is of the most general form. SPS, EPS, and DPS can be regarded as special cases of TPS modulation. Table 3.1 compares the four modulation methods. In terms of control flexibility, SPS modulation has one control degree of freedom. EPS and DPS have two, and TPS has three. Hence, TPS offers the highest flexibility of shaping the inductor current, potentially achieving the largest ZVS range, lowest circulating power and current stress, and highest efficiency. However, TPS is also the most complicated one. It requires higher computational resources from the controller and might have relatively worse dynamic performance. For SPS modulation, although ZVS range and circulating power get worse at mismatched voltages, it is still one of the most widely used modulation methods owing to its simplicity, robustness, fast dynamics, and reasonably good performance for DAB converters. The following analysis in this chapter is based on the SPS modulation method.

3.2.2 Power flow analysis

The power flow of a DAB converter can be analyzed based on the simplified model in Fig. 3.2B, in which power losses and magnetic inductance are neglected. Fig. 3.4 plots the waveforms of the equivalent source voltages (v_p and v_s/n), inductor current, and instantaneous output power. Under SPS modulation, equivalent voltage sources will generate two square-wave voltages with an amplitude of V_i and $V_o^{'}$, respectively. V_i is the input voltage and $V_o^{'} = \dfrac{V_o}{n}$ is the primary-referred output voltage. In this chapter, buck or boost operation mode refers to $V_i > V_o^{'}$ or $V_i < V_o^{'}$. Define the voltage conversion gain as $M = V_o^{'}/V_i$. In Fig. 3.4, the shaded area of the instantaneous output power is the backflow power that flows in the opposite direction of average power flow [15]. The backflow power reflects the reactive power of the DAB converter, and higher backflow power will lead to higher conduction losses.

TABLE 3.1 Comparison of four typical modulation methods.

	Single-phase shift modulation	**Extended-phase shift modulation**	**Double-phase shift modulation**	**Triple-phase shift modulation**
Controlled variable	One variable:	Two variables:	Two variables:	Three variables:
	Outer phase shift φ	Outer phase shift φ +	Outer phase shift φ +	Outer phase shift φ +
		Inner phase-shift D_E in one active bridge	Inner phase shift D_D in both active bridges	Two inner phase-shifts D_{T1s}, D_{T2} in two active bridges
Control complexity	Low	Medium	Medium	High
Pros	Simple and robust; good dynamics	Expanded ZVS range and lower circulating power	Expanded ZVS range and lower circulating power; symmetric modulation of two active bridges	Largest ZVS range and lowest circulating power
Cons	Limited ZVS range and high circulating power at mismatched voltages	Unsymmetric modulation of two active bridges; more complicated	More complicated	Most complicated

ZVS, zero-voltage switching.

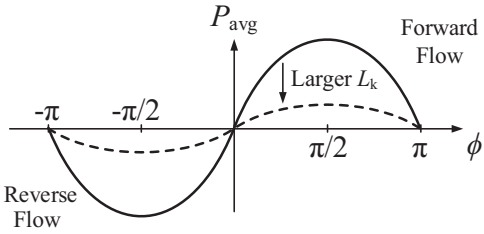

FIGURE 3.4 Average output power as a function of phase shift φ in the range of $[-\pi, \pi]$. Negative values indicate a reverse power flow from the output side to the input side.

The average output power (or active power) of one switching cycle can be derived as:

$$P_{\text{avg}} = \frac{1}{T_{hs}} \int_{t=0}^{t=t_{hs}} i_L v_p dt = \frac{1}{T_{hs}} \int_{t=0}^{t=t_{hs}} \frac{i_L v_s}{n} dt = \frac{V_i V_o{}'}{2\pi f L_k} \varphi \left(1 - \frac{|\varphi|}{\pi}\right) \tag{3.1}$$

where f is the switching frequency and T_{hs} is the half switching period. Eq. (3.1) applies to any conversion gain M and the whole PS range of $[-\pi, \pi]$. Fig. 3.5 plots the average output power as a function of PS φ. A negative PS indicates that the secondary active bridge is leading, and negative average power indicates a reverse power flow from the output side to the input side. Because $P_{\text{avg}} \propto 1/L_k$, a larger leakage inductance will reduce the maximum output power, but it might be beneficial for the control resolution of digital controllers because a higher PS value is required for the same power.

As shown in Fig. 3.5, the average power is symmetric for the forward and the reverse power flows, and its magnitude reaches the maximum at $\pm \frac{\pi}{2}$. For convenience, the following analysis is performed under the assumption of forward power flow (φ is in the range of $[0, \pi]$), but the analysis method can

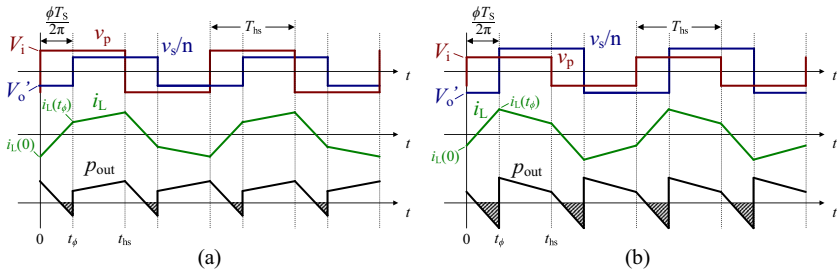

FIGURE 3.5 Waveforms of primary and secondary equivalent source voltages (v_p and v_s/n), inductor current, and instantaneous output power in: (A) Buck operation mode ($M < 1$); (B) boost operation mode ($M > 1$). *Shaded areas* of instantaneous output power are the backflow power.

easily be extended to the case of reverse power flow in the range of $[-\pi, 0]$ by swapping input and output designations.

3.2.3 Component current stresses and zero-voltage switching operation range

In power converters, the current rating of a power switch or saturation current limit of an inductor needs to be designed for its peak current value during operation, and its conduction loss is closely related to the rms current. To analyze component current stresses of the DAB converter, peak and rms values of primary-referred inductor current are analyzed, to which current stresses of other components can be linked. Assuming forward power flow (i.e., φ is in [0, π]), primary-referred inductor currents at time instants of $t = 0$ and $t = t_\varphi$ in Fig. 3.4 can be derived as:

$$i_L(0) = -\frac{V_i}{2\pi f L_k}\left(M\varphi + \frac{1-M}{2}\pi\right);\ \ i_L(t_\varphi) = \frac{V_i}{2\pi f L_k}\left(\varphi + \frac{M-1}{2}\pi\right) \tag{3.2}$$

Eq. (3.2) applies to any conversion gain M. The inductor peak current is the larger one between $i_L(0)$ and $i_L(t_\varphi)$, which differs in buck and boost operation modes:

$$I_{L,\,pk(\mathrm{Pri})} = \begin{cases} |i_L(0)| = \dfrac{V_i}{2\pi f L_k}\left(M\varphi + \dfrac{1-M}{2}\pi\right),\ M < 1 \\ |i_L(t_\varphi)| = \dfrac{V_i}{2\pi f L_k}\left(\varphi + \dfrac{M-1}{2}\pi\right),\ M \geq 1 \end{cases} \tag{3.3}$$

Eq. (3.3) indicates that the inductor peak current keeps increasing as φ increases from 0 to π, but the forward average power starts to decrease after φ becomes larger than $\pi/2$, as shown in Fig. 3.5. Although the DAB converter can still operate in the range of $[\pi/2, \pi]$, it will have a larger peak current, which requires a higher component current rating. The rms value of primary-referred inductor current can be derived as:

$$\begin{aligned} I_{L,\,\mathrm{rms(Pri)}} &= \sqrt{\frac{i_L(0)^2 + \mathrm{i}_L(t_\varphi)^2}{3} + \frac{2\varphi - \pi}{3\pi} i_L(0) i_L(t_\varphi)} \\ &= \frac{V_i}{2\pi f L_k}\sqrt{\frac{\pi^2(M-1)^2}{12} + \varphi^2\left(1 - \frac{2\varphi}{3\pi}\right)M} \end{aligned} \tag{3.4}$$

In the DAB converter, each power switch conducts the inductor current for half of a switching cycle, so the switch peak current is the same as the inductor peak current of the same side, but the switch rms current is only $1/\sqrt{2}$ of the inductor rms current. Besides, the current ratio between the primary side and secondary side is n:1 (n is the transformer turns ratio as defined in Fig. 3.2).

Accordingly, the peak and rms current values of each component in the DAB converter can be obtained and are summarized in Table 3.2, where the current stresses of other components are linked to the primary-referred inductor current.

Because rms currents of different components in the DAB converter are directly related, the inductor rms current can be used as a metric to evaluate the conduction loss or converter efficiency. As indicated by Eq. (3.4), however, the inductor rms current is determined by multiple factors including PS, conversion gain, switching frequency, and leakage inductance. A fair evaluation is to normalize the inductor rms current to the input or the output current, and the normalized inductor rms current is related only to PS φ and voltage conversion gain M. Fig. 3.6 plots the normalized secondary-referred inductor current, which is normalized to the output current, as a function of M and φ. When M deviates from unity gain, the normalized inductor rms current becomes larger, indicating that a mismatched input and output voltage of the DAB converter tends to increase the conduction loss. In fact, conversion gain and PS are closely related when designing the DAB converter for a specific application. Optimization methods can be applied to obtain the minimum normalized component rms current.

Besides conduction loss, switching loss is another major type of power loss. The DAB converter can achieve the ZVS-on of power switches, greatly reducing switching loss. However, a ZVS operation might lose under certain conditions. Fig. 3.7 demonstrates two example cases in which the active bridge of the primary or secondary side loses ZVS. The basic requirements of achieving ZVS for the DAB converter are:

$$\begin{cases} i_L(0) < 0, \text{ for primary side ZVS} \\ i_L(t_\varphi) > 0, \text{ for secondary side ZVS} \end{cases} \tag{3.5}$$

As shown in Fig. 3.7, $i_L(0)$ the buck operation mode has the peak inductor current, which is always negative if the load is not zero. Therefore, in the buck operation mode, the primary bridge can automatically achieve ZVS, but the secondary bridge might lose ZVS. Similarly, in the boost operation mode, the secondary bridge can automatically realize ZVS, whereas the primary bridge might lose it. Substituting Eq. (3.2) into Eq. (3.5), the PS ranges for achieving ZVS of all switches in buck and boost operation modes are:

$$\begin{cases} \varphi > \dfrac{\pi}{2}(1-M), \ M < 1 \\ \varphi > \dfrac{\pi}{2}\left(1-\dfrac{1}{M}\right), \ M \geq 1 \end{cases} \tag{3.6}$$

Fig. 3.8 shows the ZVS operation range versus voltage conversion gain. As indicated by the figure, if the input and the output voltages are matched (i.e., $M = 1$), ZVS can be achieved for the whole PS range (i.e., arbitrary load

TABLE 3.2 Peak and rms currents of each component in the dual active bridge converter in Fig. 3.2.

	Primary side		Secondary side	
	Inductor (or transformer winding)	Switch	Inductor (or transformer winding)	Switch
Peak current	$\begin{cases} \frac{V_i}{2\pi f L_k}\left(M\varphi + \frac{1-M}{2}\pi\right), M < 1 \\ \frac{V_i}{2\pi f L_k}\left(\varphi + \frac{M-1}{2}\pi\right), M \geq 1 \end{cases}$	$I_{L,pk(\mathrm{Pri})}$	$\frac{1}{n}I_{L,pk(\mathrm{Pri})}$	$\frac{1}{n}I_{L,pk(\mathrm{Pri})}$
Root-mean-square current	$\frac{V_i}{2\pi f L_k}\sqrt{\frac{\pi^2(M-1)^2}{12} + \varphi^2\left(1 - \frac{2\varphi}{3\pi}\right)M}$	$\frac{1}{\sqrt{2}}I_{L,\mathrm{rms(Pri)}}$	$\frac{1}{n}I_{L,\mathrm{rms(Pri)}}$	$\frac{1}{\sqrt{2}n}I_{L,\mathrm{rms(Pri)}}$

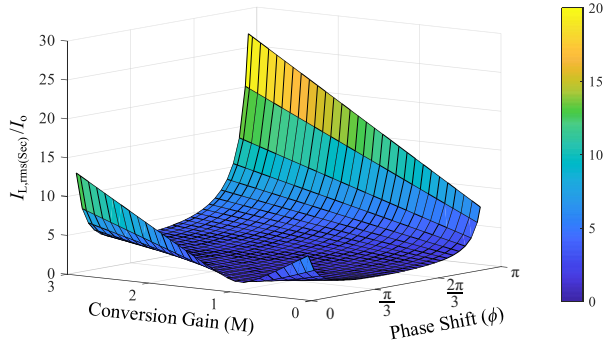

FIGURE 3.6 Normalized secondary-referred inductor current (normalized to the output current) as a function of voltage conversion gain (M) and phase shift (φ).

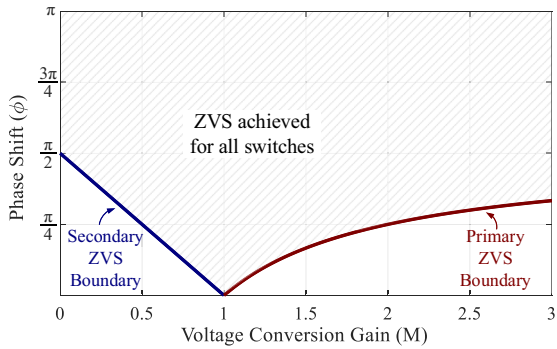

FIGURE 3.7 Zero-voltage switching (ZVS) operation range. *Blue line* is the ZVS boundary of the secondary bridge. *Red line* is the ZVS boundary of the primary bridge. *Shaded area* is the phase-shift range for achieving ZVS of all switches.

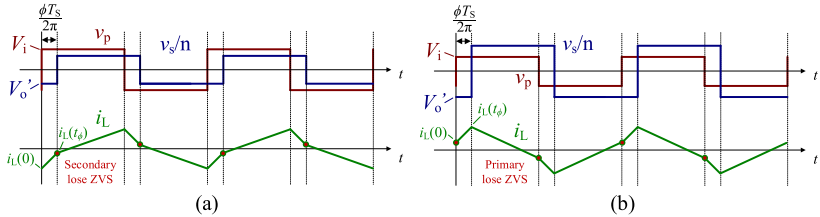

FIGURE 3.8 Example cases of losing zero-voltage switching (ZVS): (A) Secondary bridge loses ZVS in buck operation mode; (B) Primary bridge loses ZVS in boost operation mode.

power), but the ZVS range will shrink at mismatched input and output voltages. When M deviates from the unity gain, with DAB operated at light load with small PSs, it becomes easier to lose ZVS.

In practice, besides the requirements described in Eq. (3.5), energy stored in the leakage inductance should be large enough to charge and discharge the parasitic capacitances of power switches fully. Fig. 3.9 shows the current commutation at $t = 0$ and $t = t_\varphi$. For primary bridge at $t = 0$, to keep $i_L(0) < 0$ while charging and discharging parasitic capacitances, the minimum energy stored in the leakage inductance needs to fulfill:

$$\frac{1}{2} L_k i_{L,min}^2 \geq 2 C_{oss} V_i V_o^{'} \tag{3.7}$$

In Eq. (3.7), $V_o^{'} = \frac{V_o}{n}$. Here, all switches are assumed to have the same parasitic capacitance, C_{oss}, but unequal parasitic capacitances can be analyzed similarly. As for the secondary bridge at $t = t_\varphi$, the primary source is delivering power to the secondary side and is increasing the inductor current in the positive direction, so $i_L(t_\varphi) > 0$ can be automatically maintained. For both primary and secondary bridges, an appropriate deadtime is required to complete the charging and discharging process of parasitic capacitances [54].

As indicated by Fig. 3.8 and Eq. (3.7), the ZVS operation range will be reduced owing to unmatched input and output voltages and parasitic capacitances [11,55], especially under light load conditions. Increasing leakage inductance L_k can help to expand the ZVS range, because it will increase the PS and inductor energy storage, making Eqs. (3.6) and (3.7) easier to be met. However, a larger leakage inductance will lower the maximum output power and might lead to higher rms currents and conduction losses if the PS is too large. Thus, leakage inductance can be optimized based on trade-offs among the ZVS operation range, conduction losses, and output power rating.

In addition, reducing magnetizing inductance can provide a larger inductive current to expand the ZVS range, but it might suffer from lower

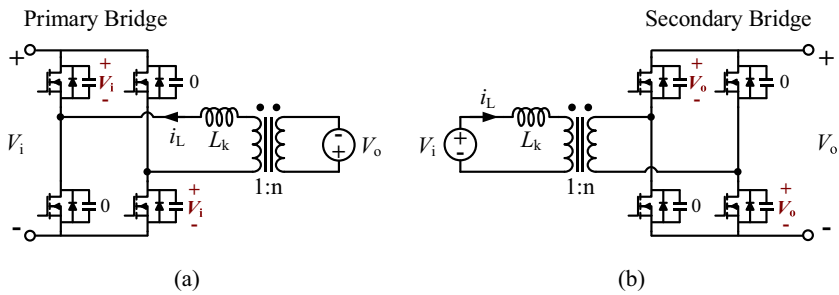

FIGURE 3.9 Equivalent circuit of the dual active bridge converter when charging and discharging switch parasitic capacitance during zero-voltage switching-on of (A) Primary bridge at $t = 0$; (B) Secondary bridge at $t = t_\varphi$.

transformer use, higher conduction loss, and lower maximum output power [55,56]. Other techniques such as frequency modulation [54,57] and various PS modulation methods [12–21,38–44] can be applied to enlarge the ZVS range with the trade-offs of control complexity.

3.3 Modeling and control for dual active bridge converter

3.3.1 Large- and small-signal modeling

To design control strategies for the DAB converter, appropriate modeling that can accurately describe the converter dynamics is required. Here, large- and small-signal modeling is developed based on SPS modulation, but the modeling methods can be extended to other modulations. The developed large- and small-signal models are verified by PLECS simulations of an example DAB with parameters listed in Table 3.3.

For DAB modeling, the conventional state-space averaging method is difficult to apply because the leakage inductor current i_L is an AC current with a zero DC component. The most common DAB modeling approach is the reduced-order model, in which the dynamics of i_L are ignored, and the switching-cycle averaged values are directly obtained for the entire converter based on active power flow [22,23]. Denote the currents that directly flow in and out of the two active bridges in Fig. 3.2 as i_p and i_s. $\langle i_p \rangle$ and $\langle i_s \rangle$ are their switching-cycle averaged values [58]. According to Eq. (3.1), $\langle i_p \rangle$ and $\langle i_s \rangle$ can be derived as:

$$\begin{cases} \langle i_p \rangle = \dfrac{P_{avg}}{v_i} = \dfrac{v_o}{2\pi f n L_k} \varphi \left(1 - \dfrac{|\varphi|}{\pi}\right) \\ \langle i_s \rangle = \dfrac{P_{avg}}{v_o} = \dfrac{v_i}{2\pi f n L_k} \varphi \left(1 - \dfrac{|\varphi|}{\pi}\right) \end{cases} \tag{3.8}$$

TABLE 3.3 Parameters of example dual active bridge for large- and small-signal modeling verification.

Parameter	Value
Input voltage, V_i	380 V
Output voltage, V_o	800 V
Transformer turns ratio, n	2
Leakage inductance, L_k	20 μH
Output capacitor, C_o	2 mF
Load resistor, R_L	50 Ω
Switching frequency, f	20 kHz

Eq. (3.8) shows that the DAB converter can be modeled as two controlled current sources for the input and output sides. Therefore, the large-signal circuit of the reduced-order model can be plotted as Fig. 3.10A. Fig. 3.11 compares the large-signal model with the simulation results of the example DAB during an input voltage step change and a PS step change. As shown in the figure, the output voltage $\langle V_o \rangle$ and current $\langle i_s \rangle$ match precisely, validating the large-signal model.

The small-signal current of $\langle i_s \rangle$ can be obtained from Eq. (3.8) as:

$$\hat{i_s} = G_{vi}\hat{v_i} + G_{\varphi i}\hat{\varphi}, \tag{3.9}$$

$$\begin{cases} G_{vi} = \dfrac{1}{2\pi f n L_k}\Phi\left(1 - \dfrac{|\Phi|}{\pi}\right) \\ G_{\varphi i} = \dfrac{V_i}{2\pi f n L_k}\left(1 - \dfrac{2|\Phi|}{\pi}\right) \end{cases} \tag{3.10}$$

where $\hat{v_i}$ and $\hat{\varphi}$ are perturbations of input voltage and PS: $v_i = \hat{v_i} + V_i$; $\varphi = \Phi + \hat{\varphi}$. Eq. (3.9) implies that the small-signal current $\hat{i_s}$ is a function of perturbations $\hat{v_i}$ and $\hat{\varphi}$, and the corresponding small-signal model at the output side can be plotted as Fig. 3.10B. In the small-signal model, $\hat{v_o}$ and $\hat{i_s}$ are

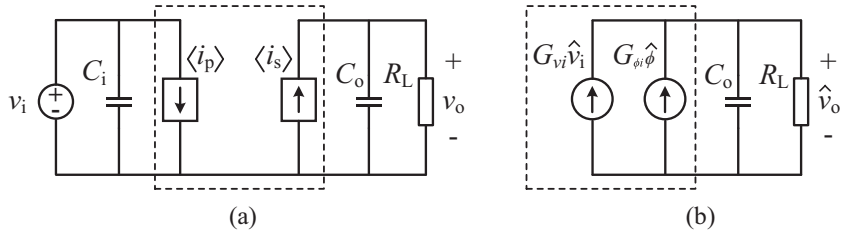

FIGURE 3.10 Reduced-order model of dual active bridge in Fig. 3.2: (A) Large-signal model; (B) small-signal model.

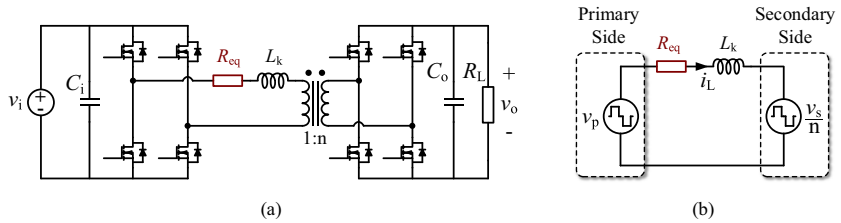

FIGURE 3.11 Dual active bridge (DAB) converter when considering power loss: (A) DAB circuit with an equivalent resistance R_{eq} capturing the conduction losses of power switches, leakage inductor, and transformer windings; (B) Simplified DAB model.

linked by the load impedance $Z_L = R_L \| \frac{1}{sC_o}$. Ignoring the input voltage perturbation, the control ($\widehat{\varphi}$) to output ($\widehat{v_o}$) transfer function is:

$$G_{\varphi v} = \frac{\widehat{v_o}}{\widehat{\varphi}} = \frac{\widehat{i_s} \times Z_L}{\widehat{\varphi}} = \frac{V_i}{2\pi f n L_k}\left(1 - \frac{2|\Phi|}{\pi}\right) \times \frac{R_L}{R_L C_o s + 1} \tag{3.11}$$

Eq. (3.11) indicates that the reduced-order model of the DAB is a first-order system. The pole of the transfer function is determined only by load impedance Z_L. This reduced-order modeling method can be further applied to other modulations (e.g., TPS [59]) by modifying their corresponding gain, $G_{\varphi i}$.

Eq. (3.11) is developed assuming a lossless DAB. In practice, DAB power losses will also influence the transfer function [24,25]. Thus, we consider conduction losses to improve the small-signal model. Fig. 3.12 plots a DAB circuit and its simplified model with a lumped resistance, R_{eq}, capturing the conduction losses of power switches, leakage inductor, and transformer windings. The R_{eq} together with L_k leads to a piecewise exponential current waveform, as shown in Fig. 3.13A. The exponential waveform will raise the peak and rms values of the inductor current, increasing the component current ratings and DAB power losses. It will also affect the average output power, so Eqs. (3.8)−(3.11) are no longer valid. However, the reduced-order model can still be applied by calculating the half-cycle averaged value of the exponential current. As a result, the DAB small-signal model when considering conduction losses can be obtained, as shown in Fig. 3.13B, where the R_{eq} brings about output resistance R_o and modified gains $G_{vi}{}', G_{\varphi i}{}'$:

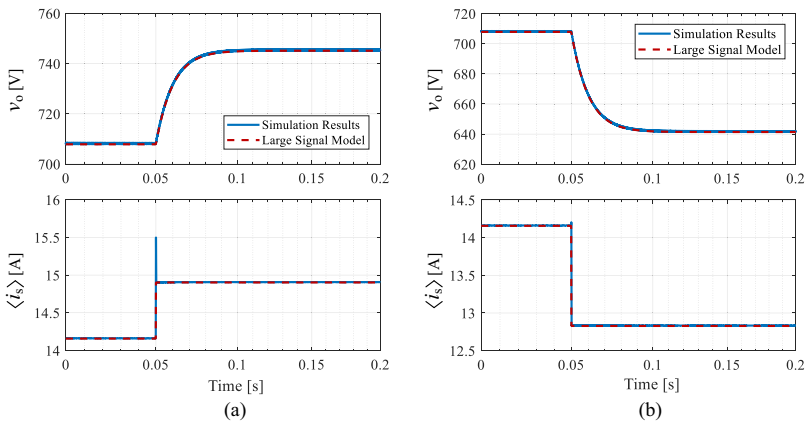

FIGURE 3.12 Comparison of large-signal model and simulation results when (A) input voltage V_i changes from 380 to 400 V and (B) phase shift $\boldsymbol{\varphi}$ changes from 0.2 to 0.18. Output capacitance $C_o = 200$ μF is used in this simulation.

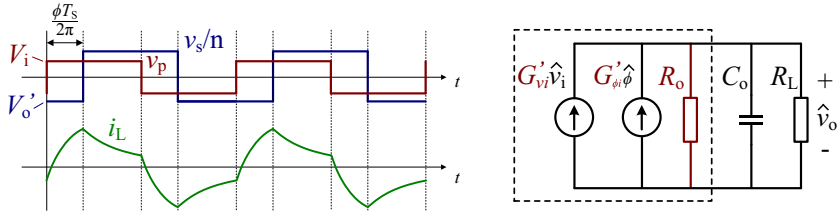

(a) (b)

FIGURE 3.13 Dual active bridge converter when considering power loss: (A) Operation waveforms; (B) Small-signal circuit model.

$$R_o = \frac{n^2 R_{eq}}{1 - \dfrac{4\tau\left(1 - \exp\left(-\frac{T}{2\tau}\right)\right)}{T\left(1 + \exp\left(-\frac{T}{2\tau}\right)\right)}} \tag{3.12}$$

$$\begin{cases} G_{vi}{}' = \dfrac{1}{n}\left(\dfrac{1}{R_{eq}}\left(1 - \dfrac{2\varphi}{\pi}\right) + \dfrac{4\tau\left(1 + \exp\left(-\dfrac{T}{2\tau}\right) - 2\exp\left(-\dfrac{\varphi T}{2\pi\tau}\right)\right)}{TR_{eq}\left(1 + \exp\left(-\dfrac{T}{2\tau}\right)\right)}\right) \\ G_{\varphi i}{}' = \dfrac{V_i}{n\pi}\left(\dfrac{-2}{R_{eq}} + \dfrac{4\exp\left(-\dfrac{\varphi T}{2\pi\tau}\right)}{R_{eq}\left(1 + \exp\left(-\dfrac{T}{2\tau}\right)\right)}\right) \end{cases} \tag{3.13}$$

$\tau = \frac{L_k}{R_{eq}}$ is the time constant of the L-R circuit, and φ is the PS at the DC operating point (assume $\varphi > 0$). Detailed derivations can be found in Zhang et al. [24] and Wang et al. [25]. The improved control to output transfer function can be derived as:

$$G_{\varphi v}{}' = \frac{\hat{v_o}}{\hat{\varphi}} = \frac{\hat{i_s} \times (Z_L \| R_o)}{\hat{\varphi}} = G_{\varphi i}{}' \times \frac{(R_L \| R_o)}{(R_L \| R_o) C_o s + 1} \tag{3.14}$$

Fig. 3.14 plots the control to output transfer function of the example DAB with and without power losses. The precisely matched simulated and calculated results validate the small-signal models in both cases. Fig. 3.14 also implies that power losses of the DAB converter will reduce the gain and the crossover frequency of the control to output transfer function. An appropriate compensation network might be needed in the control loop design to compensate for the gain and bandwidth, to achieve a faster response.

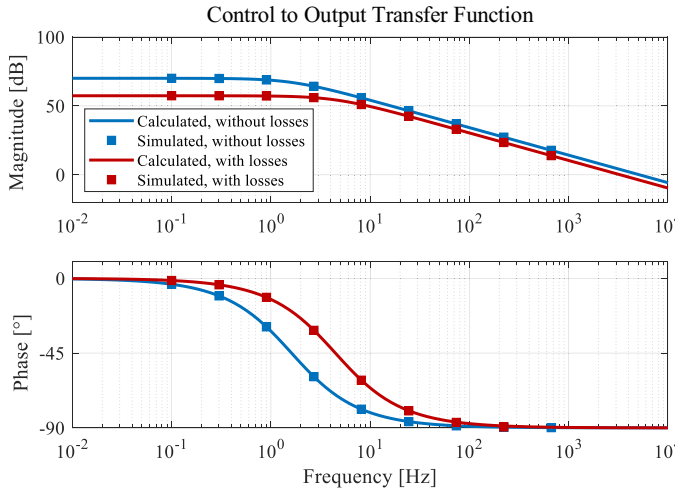

FIGURE 3.14 Control to output transfer function of example dual active bridge converter with and without losses. In the case of considering conduction losses, $R_{eq} = 1.5\ \Omega$.

Apart from the reduced-order model, other DAB modeling methods such as the generalized average model [26–28] and discrete-time model [29–31] have been widely studied. Different modeling methods are compared in Shao et al. [33] in terms of the model accuracy and complexity. Although the reduced-order model ignores the dynamics of leakage inductor current, it has high accuracy with the lowest model complexity, making it a great fit for the controller design.

3.3.2 Output voltage control

Fig. 3.10 implies that the DAB converter can be equivalent to a current source. Its output current depends on the PS and the input voltage, irrelevant to the output voltage. Many applications, however, require a regulated voltage for normal functioning, and thus a proper output voltage control strategy is needed. Shao et al. [33] introduced and compared various output voltage control strategies for the DAB converter. In this chapter, two common methods, output voltage feedback control and output voltage feedback plus output current feedforward control, are presented. Their control loops are designed for an example DAB, as listed in Table 3.4, and their performance in terms of dynamic response and the rejection of load current disturbance is discussed.

Output voltage feedback control is a simple, effective, and robust method of regulating the output voltage. Fig. 3.15 plots the block diagram of the output voltage feedback control, in which a feedback loop is constructed from the

TABLE 3.4 Parameters of example dual active bridge for control loop design.

Parameter	Value
Input voltage, V_i	400 V
Output voltage, V_o	50 V
Transformer turns ratio, n	1/8
Leakage inductance, L_k	40 μH
Output capacitor, C_o	250 μF
Load resistor, R_L	1.25 Ω
Switching frequency, f	100 kHz

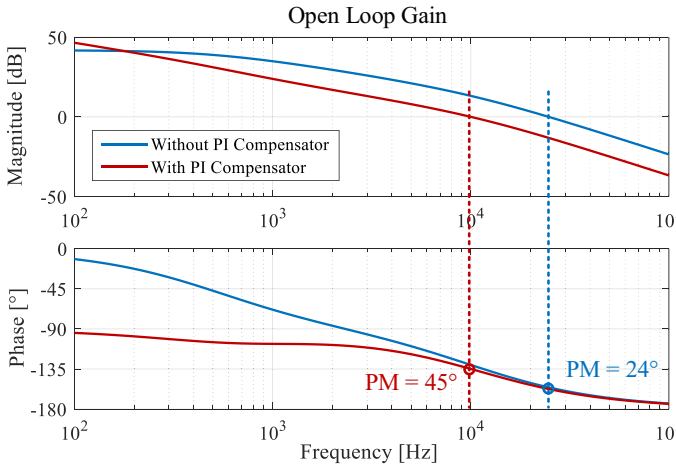

FIGURE 3.15 Bode plot of open loop gain with and without PI compensator. After PI compensation, the phase margin is adjusted to 45 degrees at the crossover frequency of 10 kHz.

sampled output voltage. The PS of the DAB is adjusted based on the difference between the sampled and reference voltage values. A PI compensator, $G_C = K_p + \frac{K_i}{s}$, can be used to eliminate the steady-state control error and balance the bandwidth and phase margin of the control loop. The open loop gain of the output voltage feedback control in Fig. 3.15 is given as:

$$Loop\ gain = G_C G_{\varphi i} Z_L\, e^{-1.5Ts} \tag{3.15}$$

Here, a delay term, $e^{-1.5Ts}$, is added to model the time delay caused by sampling and PS updating in a digital controller. Fig. 3.16 plots the bode plot of the open loop gain designed for the example DAB in Table 3.4. PI parameters are adjusted to have a 45-degree phase margin at a 10-kHz crossover frequency for the 1.25-Ω load resistance (i.e., 2 kW load power), so $K_p = 0.219, K_i = 1090$. Obviously, a trade-off exists between transient speed and stability: the higher the phase margin, the lower the crossover frequency becomes. Accordingly, the closed loop transfer function is:

$$\text{Transfer function} = \frac{\widehat{v}_o}{\widehat{v}_{\text{ref}}} = \frac{G_C G_{\varphi i} Z_L \, e^{-1.5Ts}}{1 + G_C G_{\varphi i} Z_L \, e^{-1.5Ts}} \tag{3.16}$$

For a DAB converter under a closed loop control, its output impedance, Z_o, can be used as a metric to evaluate the ability to reject the load disturbance, which determines the output voltage transients during a load change. A lower output impedance indicates a higher load disturbance rejection capability. Fig. 3.17 plots the equivalent circuit and block diagram for evaluating Z_o. An output current disturbance, $\widehat{i}_{ac}$, is applied at a DC operating point indicated by a constant current source, I_{dc}. The corresponding small-signal output voltage is observed, and Z_o for the DAB with output voltage feedback control can be obtained as:

$$Z_o = \frac{\widehat{v}_o}{\widehat{i}_{ac}} = \frac{1}{C_o s + G_C G_{\varphi i} \, e^{-1.5Ts}} \tag{3.17}$$

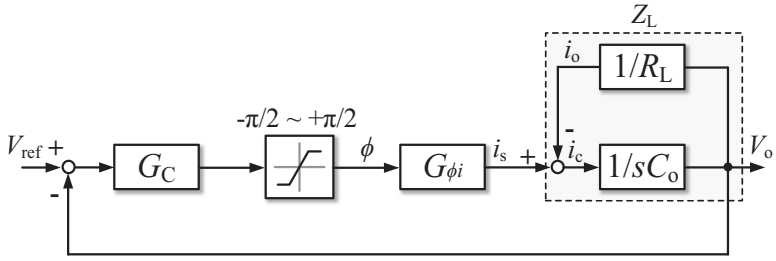

FIGURE 3.16 Block diagram of output voltage feedback control for dual active bridge converter.

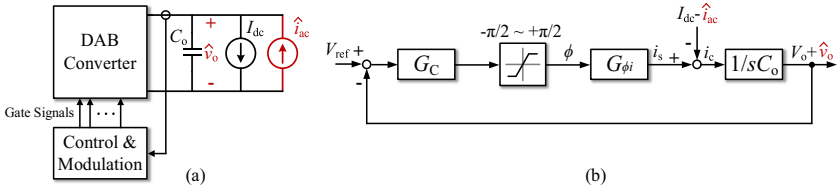

FIGURE 3.17 Output impedance evaluation for dual active bridge (DAB) with closed loop control: (A) Evaluation circuit; (B) equivalent block diagram.

Fig. 3.18 shows the bode plots of the closed loop transfer function and output impedance. When load resistance $R_L = 1.25\ \Omega$, the 3-dB bandwidth is about 160 kHz for this design and the maximum output impedance is about 0.09 Ω. As the R_L increases from 1.25 to 100 Ω (i.e., P_{out} drops from 2 kW to 25 W), both the closed loop transfer function and the output impedance do not change much, indicating that the performance of the output voltage feedback control is robust to the operating points. To validate the control strategy, the

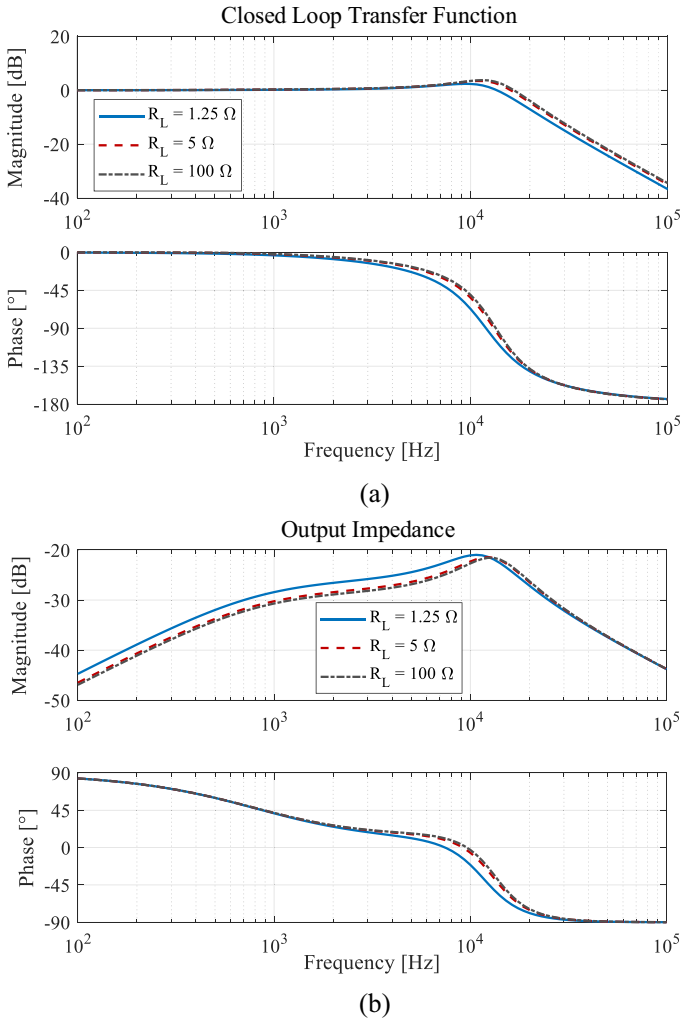

FIGURE 3.18 Bode plots of output voltage feedback control under different load conditions: (A) Closed loop transfer function; (B) output impedance.

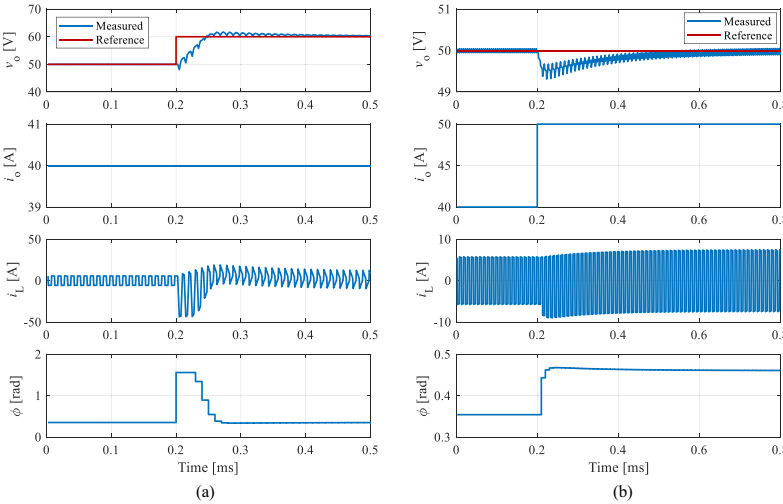

FIGURE 3.19 Transient response under the output voltage feedback control when (A) reference voltage changes from 50 to 60 V, and (B) load current changes from 40 to 50 A.

example DAB with output voltage feedback control is built in PLECS. PS is updated once per switching cycle to simulate the digital controller. Fig. 3.19 shows the operation waveforms during the transients of reference voltage step change and load current step change. Under this closed loop control, the DAB converter can closely track the reference voltage or maintain stable output voltage during the load current step change.

An improved control strategy is the output voltage feedback plus output current feedforward control. The output current feedforward path can sense the load disturbance and have a quick response on the PS to counteract the influence of load change on the output voltage, decreasing the output impedance. Based on Eq. (3.1), the expected PS can be expressed as a function of the input voltage V_i and load current i_o:

$$\Phi_{\text{exp}} = \begin{cases} \dfrac{\pi}{2} - \dfrac{\pi}{2}\sqrt{1 - \dfrac{8nfL_k}{V_i} i_o}, & i_o > 0 \\ -\dfrac{\pi}{2} + \dfrac{\pi}{2}\sqrt{1 + \dfrac{8nfL_k}{V_i} i_o}, & i_o < 0 \end{cases} \tag{3.18}$$

Fig. 3.20 shows the block diagram of the output voltage feedback plus output current feedforward control strategy. As indicated in the figure, an expected PS will be calculated through Eq. (3.18) with the real-time sampled V_i and i_o. The expected phase shift plus the output of the PI compensator sends

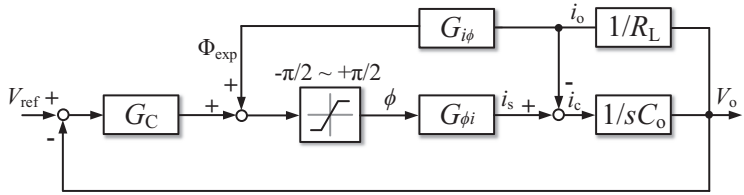

FIGURE 3.20 Block diagram of output voltage feedback plus output current feedforward control.

the PS command to the DAB converter. To obtain the small-signal transfer function, Eq. (3.18) needs to be linearized as:

$$G_{i\varphi} = \frac{d\varphi}{di_o} = \frac{2\pi fnL_k}{V_i}\left(1 - \frac{8nfL_k}{V_i}|I_o|\right)^{-\frac{1}{2}} \tag{3.19}$$

where I_o is the load current of the DC operating point. Based on Eq. (3.19), the block diagram in Fig. 3.20 can be reorganized into Fig. 3.21, and the closed loop transfer function can be derived as:

$$\text{Transfer function} = \frac{\widehat{v}_o}{\widehat{v}_{\text{ref}}} = \frac{G_C G_{\varphi i} Z_L\, e^{-1.5Ts}}{1 + \left(G_C G_{\varphi i} - G_{i\varphi} G_{\varphi i}/R_L\right) Z_L\, e^{-1.5Ts}} \tag{3.20}$$

Output impedance Z_o is measured in the same way as in Fig. 3.17A, and its block diagram is plotted in Fig. 3.22. Consequently, Z_o of the DAB with output voltage feedback plus output current feed forward control can be derived as:

$$Z_o = \frac{\widehat{v}_o}{\widehat{i}_{ac}} = \frac{1 - G_{i\varphi} G_{\varphi i} e^{-1.5Ts}}{C_{\text{out}} s + G_C G_{\varphi i}\, e^{-1.5Ts}} \tag{3.21}$$

Ideally, $G_{i\varphi} G_{\varphi i}$ is equal to 1 according to Eqs. (3.10) and (3.19). Therefore, Z_o can be significantly reduced, even to zero if the delay is negligible. However, the L_k value in $G_{\varphi i}$ is the actual leakage inductance, because $G_{\varphi i}$ is

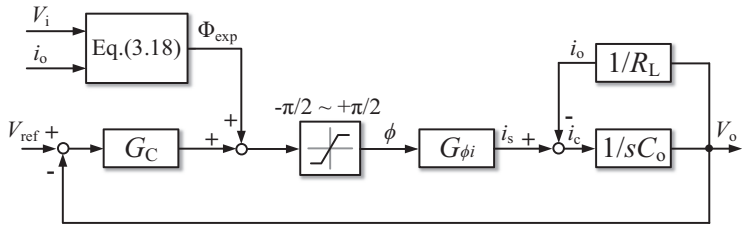

FIGURE 3.21 Reorganized block diagram of output voltage feedback plus output current feedforward control.

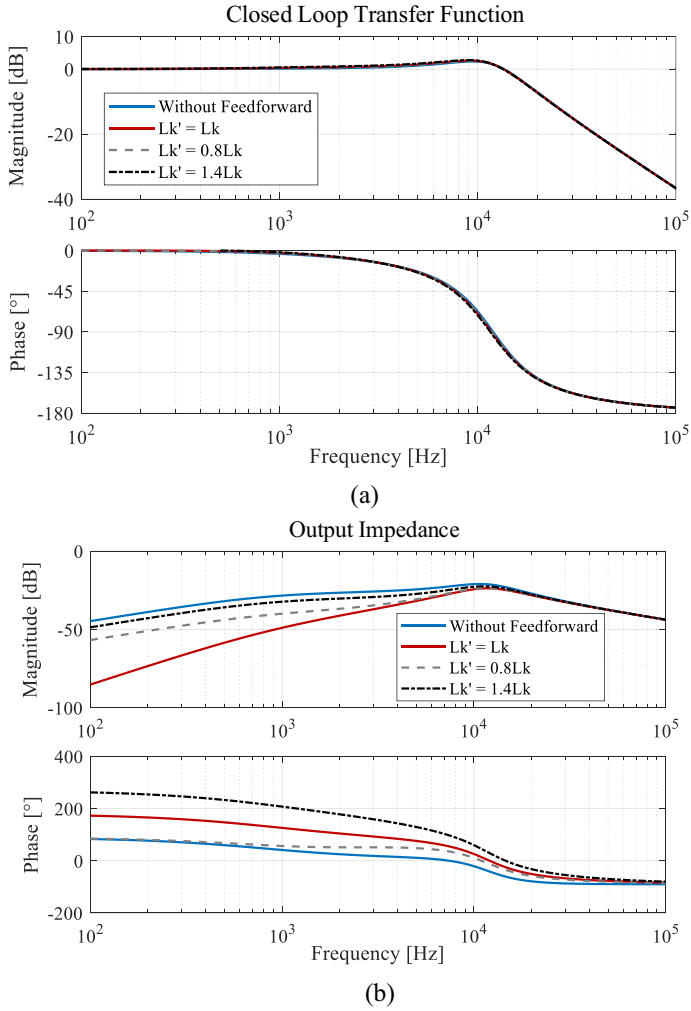

FIGURE 3.22 Bode plots of output voltage feedback plus output current feedforward with different mismatched leakage inductance: (A) Closed loop transfer function; (B) output impedance.

the actual control to output dynamics of the converter. whereas in $G_{i\varphi}$, the L_k value is the previously known inductance used for calculation and could be different from the actual value. The difference between the previously known leakage inductance and the actual leakage inductance causes $G_{i\varphi}G_{\varphi i}$ to deviate 1, which will deteriorate the control performance. Denote the previously

known leakage inductance as $L_k^{'}$. Assume $L_k^{'} = \alpha L_k$. Based on Eqs. (3.8) and (3.19), $G_{i\varphi}$ can be reorganized as:

$$G_{i\varphi}^{'} = \frac{2\pi fn\alpha L_k}{V_i}\left(1 - \frac{8nf\alpha L_k}{V_i}|I_o|\right)^{-\frac{1}{2}} = \frac{2\pi fn\alpha L_k}{V_i}\left[1 - \frac{4\alpha}{\pi}\left(|\Phi| - \frac{\Phi^2}{\pi}\right)\right]^{-\frac{1}{2}} \tag{3.22}$$

Substituting Eq. (3.22) into Eqs. (3.20) and (3.21), the closed loop transfer function and output impedance when the previously known leakage inductance mismatches with the actual value can be obtained.

Fig. 3.23 shows the bode plots of the transfer function and output impedance with different mismatched leakage inductance values. Here, PI parameters are the same as in the output voltage feedback control: $K_p = 0.219, K_i = 1090$. Bode plots with only the output voltage feedback are plotted as a reference. As indicated in the figure, the closed loop transfer function of feedback plus feedforward control is nearly the same as that of the feedback-only control and mismatched leakage inductance has minor impacts. For the output impedance, the feedback plus feedforward control can greatly reduce the Z_o magnitude when the previously known leakage inductance matches the actual value, but Z_o will increase if the previously known and actual values are mismatched. Fig. 3.23B shows that the Z_o magnitude becomes almost the same as in the feedback-only control when $L_K^{'} = 1.4L_k$. Therefore, an accurate estimate of the actual leakage inductance is required to take full advantage of the output voltage feedback plus output current feedforward control.

Fig. 3.24 plots the simulated transient response of the feedback plus feedforward control. In the simulation, the estimated leakage inductance is selected as $L_k' = 1.1\ L_k$, and the PS is updated once per switching cycle. Fig. 3.24 implies that the transient performance of tracking reference voltage is similar to that of the feedback-only control, consistent with the discussion about the closed loop transfer function. However, the feedback plus

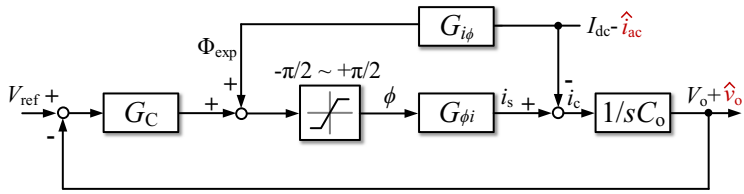

FIGURE 3.23 Block diagram of output impedance measurement for output voltage feedback plus output current feedforward control.

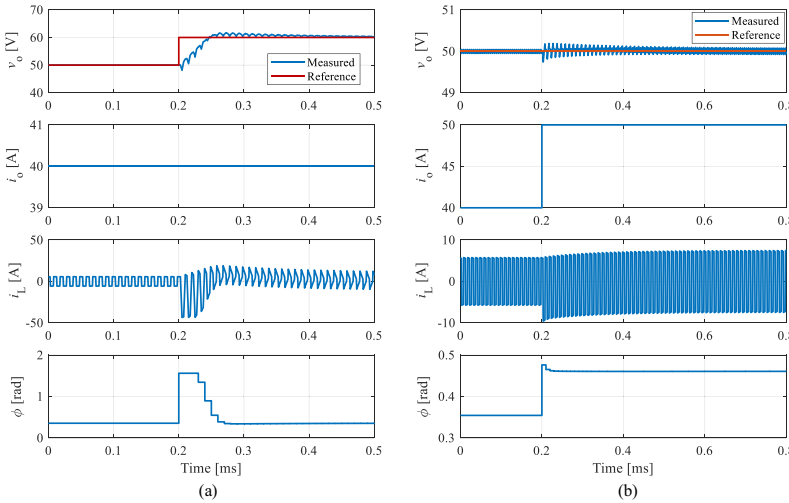

FIGURE 3.24 Transient response under output voltage feedback plus output current feedforward control when: (A) Reference voltage changes from 50 to 60 V; and (B) Load current changes from 40 to 50 A.

feedforward control can greatly improve the load disturbance rejection capability, so the output voltage can remain much more stable during the load current step change.

3.4 Summary

This chapter introduced and compared four typical modulation schemes for the DAB converter. Based on the SPS modulation, active and reactive power flows were analyzed, and specific ZVS operation range as well as component rms and peak current stresses were derived. The analysis indicated that unmatched input and output voltages and parasitic capacitances will reduce the ZVS operation range. Increasing the leakage inductance can enlarge the ZVS range but might result in larger conduction losses and a reduced output power rating. A detailed discussion about trade-offs among the ZVS range, component current stress, and output power rating was presented, providing guidance for optimizing leakage inductance.

To design the closed loop control, large- and small-signal circuits of the reduced-order model were developed and verified in a PLECS simulation. The small-signal model that captured power losses was also derived. The bode plot implied that conduction losses will reduce the gain and crossover frequency of the control to output transfer function, which needs to be compensated for in the loop design. Two closed loop control strategies, output voltage feedback

and output voltage feedback plus output current feedforward, were designed for an example DAB converter and were verified in PLECS. Their performance in terms of reference voltage tracking and load disturbance rejection was compared. The feedback plus feedforward control has a reference voltage tracking capability similar to that of the feedback-only control, but it has better load disturbance rejection capability owing to smaller output impedance. However, an accurate estimation of the actual leakage inductance is needed to take full advantage of the feedback plus feedforward control.

References

[1] IRENA, Renewable Capacity Statistics 2017, International Renewable Energy Agency (IRENA), Abu Dhabi, 2017, ISBN 978-92-9260-018-1.

[2] Z. Guo, D. Sha, X. Liao, Energy management by using point of common coupling frequency as an agent for islanded microgrids, IET Power Electron. 7 (8) (August 2014) 2111−2122.

[3] Y. Xu, C.W. Singh, Power system reliability impact of energy storage integration with intelligent operation strategy, IEEE Trans. Smart Grid 5 (2) (March 2014) 1129−1137.

[4] T. Dragičević, X. Lu, J.C. Vasquez, J.M. Guerrero, DC microgrids—Part I: a review of control strategies and stabilization techniques, IEEE Trans. Power Electron. 31 (7) (July 2016) 4876−4891.

[5] R.M. Cuzner, V. Singh, Future shipboard MVdc system protection requirements and solid-state protective device topological tradeoffs, IEEE J. Emerg. Sel. Top. Power Electron. 5 (1) (March 2017) 244−259.

[6] T.-F. Wu, C.-L. Kuo, L.-C. Lin, Y.-K. Chen, DC-bus voltage regulation for a DC distribution system with a single-phase bidirectional inverter, IEEE J. Emerg. Sel. Top. Power Electron. 4 (1) (March 2016) 210−220.

[7] D. Boroyevich, I. Cvetković, D. Dong, R. Burgos, F. Wang, F. Lee, Future electronic power distribution systems a contemplative view, in: 2010 12th International Conference on Optimization of Electrical and Electronic Equipment, May 2010, pp. 1369−1380.

[8] A.Q. Huang, M.L. Crow, G.T. Heydt, J.P. Zheng, S.J. Dale, The future renewable electric energy delivery and management (FREEDM) system: the energy internet, Proc. IEEE 99 (1) (January 2011) 133−148.

[9] B. Zhao, Q. Song, J. Li, W. Liu, A modular multilevel dc-link front-to-front dc solid-state transformer based on high-frequency dual active phase shift for HVDC grid integration, IEEE Trans. Ind. Electron. 64 (11) (November 2017) 8919−8927.

[10] R.W. De Doncker, D.M. Divan, M.H. Kheraluwala, A three-phase soft-switched high-power-density DC/DC converter for high-power applications, IEEE Trans. Ind. Appl. 27 (1) (January-February 1991) 63−73.

[11] S. Inoue, H. Akagi, A bidirectional DC−DC converter for an energy storage system with galvanic isolation, IEEE Trans. Power Electron. 22 (6) (November 2007) 2299−2306.

[12] G.G. Oggier, R. Leidhold, G.O. Garcia, A.R. Oliva, J.C. Balda, F. Barlow, Extending the ZVS operating range of dual active bridge high-power DC-DC converters, in: 2006 37th IEEE Power Electronics Specialists Conference, 2006.

[13] G.G. Oggier, G.O. GarcÍa, A.R. Oliva, Switching control strategy to minimize dual active bridge converter losses, IEEE Trans. Power Electron. 24 (7) (July 2009) 1826−1838.

[14] G. Oggier, G.O. García, A.R. Oliva, Modulation strategy to operate the dual active bridge DC-DC converter under soft switching in the whole operating range, IEEE Trans. Power Electron. 26 (4) (April 2011) 1228−1236.
[15] B. Zhao, Q. Yu, W. Sun, Extended-phase-shift control of isolated bidirectional DC−DC converter for power distribution in microgrid, IEEE Trans. Power Electron. 27 (11) (November 2012) 4667−4680.
[16] H. Bai, C. Mi, Eliminate reactive power and increase system efficiency of isolated bidirectional dual-active-bridge DC−DC converters using novel dual-phase-shift control, IEEE Trans. Power Electron. 23 (6) (November 2008) 2905−2914.
[17] M. Kim, M. Rosekeit, S. Sul, R.W. De Doncker, A dual-phase-shift control strategy for dual-active-bridge DC-DC converter in wide voltage range, in: 8th International Conference on Power Electronics - ECCE Asia, 2011, pp. 364−371.
[18] B. Zhao, Q. Song, W. Liu, Power characterization of isolated bidirectional dual-active-bridge DC−DC converter with dual-phase-shift control, IEEE Trans. Power Electron. 27 (9) (September 2012) 4172−4176.
[19] H. Zhou, A.M. Khambadkone, Hybrid modulation for dual-active-bridge bidirectional converter with extended power range for ultracapacitor application, IEEE Trans. Ind. Appl. 45 (4) (July-August 2009) 1434−1442.
[20] A.K. Jain, R. Ayyanar, PWM control of dual active bridge: comprehensive analysis and experimental verification, IEEE Trans. Power Electron. 26 (4) (April 2011) 1215−1227.
[21] F. Krismer, J.W. Kolar, Closed form solution for minimum conduction loss modulation of DAB converters, IEEE Trans. Power Electron. 27 (1) (January 2012) 174−188.
[22] H. Bai, C. Mi, C. Wang, S. Gargies, The dynamic model and hybrid phase-shift control of a dual-active-bridge converter, in: 2008 34th Annual Conference of IEEE Industrial Electronics, 2008, pp. 2840−2845.
[23] A.R. Rodríguez Alonso, J. Sebastian, D.G. Lamar, M.M. Hernando, A. Vazquez, An overall study of a Dual Active Bridge for bidirectional DC/DC conversion, in: 2010 IEEE Energy Conversion Congress and Exposition, 2010, pp. 1129−1135.
[24] K. Zhang, Z. Shan, J. Jatskevich, Large- and small-signal average-value modeling of dual-active-bridge DC−DC converter considering power losses, IEEE Trans. Power Electron. 32 (3) (March 2017) 1964−1974.
[25] P. Wang, Y. Chen, Y. Elasser, M. Chen, Small signal model for very-large-scale multi-active-bridge differential power processing (MAB-DPP) architecture, in: 2019 20th Workshop on Control and Modeling for Power Electronics (COMPEL), 2019, pp. 1−8.
[26] H. Qin, J.W. Kimball, Generalized average modeling of dual active bridge DC−DC converter, IEEE Trans. Power Electron. 27 (4) (April 2012) 2078−2084.
[27] D. Segaran, D.G. Holmes, B.P. McGrath, Enhanced load step response for a bidirectional DC−DC converter, IEEE Trans. Power Electron. 28 (1) (January 2013) 371−379.
[28] B. Liu, P. Davari, F. Blaabjerg, An enhanced generalized average modeling of dual active bridge converters, in: 2020 IEEE Applied Power Electronics Conference and Exposition (APEC), 2020, pp. 85−90.
[29] C. Zhao, S.D. Round, J.W. Kolar, Full-order averaging modelling of zero-voltage-switching phase-shift bidirectional dc-dc converters, IET Power Electron. 3 (3) (May 2010) 400−410.
[30] F. Krismer, J.W. Kolar, Accurate small-signal model for the digital control of an automotive bidirectional dual active bridge, IEEE Trans. Power Electron. 24 (12) (December 2009) 2756−2768.

[31] D. Costinett, R. Zane, D. Maksimovic, Discrete-time small-signal modeling of a 1 MHz efficiency-optimized dual active bridge converter with varying load, in: 2012 IEEE 13th Workshop on Control and Modeling for Power Electronics (COMPEL), June 2012.

[32] H. Qin, J.W. Kimball, Closed-loop control of dc-dc dual-active-bridge converters driving single-phase inverters, IEEE Trans. Power Electron. 29 (2) (February 2014) 1006−1017.

[33] S. Shao, L. Chen, Z. Shan, F. Gao, H. Chen, D. Sha, T. Dragicevic, Modeling and advanced control of dual active bridge DC-DC converters: a review, IEEE Trans. Power Electron. 37 (2) (February 2022) 1524−1547.

[34] B. Liu, P. Davari, F. Blaabjerg, An optimized hybrid modulation scheme for reducing conduction losses in dual active bridge converters, IEEE J. Emerg. Sel. Top. Power Electron. 9 (1) (February 2021) 921−936.

[35] Z. Qin, Y. Shen, P.C. Loh, H. Wang, F. Blaabjerg, A dual active bridge converter with an extended high-efficiency range by DC blocking capacitor voltage control, IEEE Trans. Power Electron. 33 (7) (July 2018) 5949−5966.

[36] Y. Shi, R. Li, Y. Xue, H. Li, Optimized operation of current-fed dual active bridge DC−DC converter for PV applications, IEEE Trans. Ind. Electron. 62 (11) (November 2015) 6986−6995.

[37] Y. Tang, W. Hu, D. Cao, N. Hou, Y. Li, Z. Chen, F. Blaabjerg, Artificial intelligence-aided minimum reactive power control for the DAB converter based on harmonic analysis method, IEEE Trans. Power Electron. 36 (9) (September 2021) 9704−9710.

[38] N. Hou, Y.W. Li, Overview and comparison of modulation and control strategies for a nonresonant single-phase dual-active-bridge DC−DC converter, IEEE Trans. Power Electron. 35 (3) (March 2020) 3148−3172.

[39] S. Shao, M. Jiang, W. Ye, Y. Li, J. Zhang, K. Sheng, Optimal phase-shift control to minimize reactive power for a dual active bridge dc−dc converter, IEEE Trans. Power Electron. 34 (10) (October 2019) 10193−10205.

[40] S. Shao, H. Chen, X. Wu, J. Zhang, K. Sheng, Circulating current and ZVS-on of a dual active bridge DC-DC converter: a review, in: IEEE Access, vol. 7, 2019, pp. 50561−50572.

[41] J. Huang, Y. Wang, Z. Li, W. Lei, Unified triple-phase-shift control to minimize current stress and achieve full soft-switching of isolated bidirectional dc−dc converter, IEEE Trans. Ind. Electron. 63 (7) (July 2016) 4169−4179.

[42] G. Xu, D. Sha, J. Zhang, X. Liao, Unified boundary trapezoidal modulation control utilizing fixed duty cycle compensation and magnetizing current design for dual active bridge dc−dc converter, IEEE Trans. Power Electron. 32 (3) (March 2017) 2243−2252.

[43] F. Krismer, J.W. Kolar, Efficiency-optimized high-current dual active bridge converter for automotive applications, IEEE Trans. Ind. Electron. 59 (7) (July 2012) 2745−2760.

[44] K. Wu, C.W. Silva, W.G. Dunford, Stability analysis of isolated bidirectional dual active full-bridge dc-dc converter with triple phase-shift control, IEEE Trans. Power Electron. 27 (4) (April 2012) 2007−2017.

[45] L. Xue, Z. Shen, D. Boroyevich, P. Mattavelli, D. Diaz, Dual active bridge-based battery charger for plug-in hybrid electric vehicle with charging current containing low frequency ripple, IEEE Trans. Power Electron. 30 (12) (December 2015) 7299−7307.

[46] B. Zhao, Q. Song, W. Liu, Y. Xiao, Next-generation multi-functional modular intelligent UPS system for smart grid, IEEE Trans. Ind. Electron. 60 (9) (September 2013) 3602−3618.

[47] E. Candan, P.S. Shenoy, R.C.N. Pilawa-Podgurski, A series-stacked power delivery architecture with isolated differential power conversion for data centers, IEEE Trans. Power Electron. 31 (5) (May 2016) 3690−3703.

[48] M. Evzelman, M.M. Ur Rehman, K. Hathaway, R. Zane, D. Costinett, D. Maksimovic, Active balancing system for electric vehicles with incorporated low-voltage bus, IEEE Trans. Power Electron. 31 (11) (November 2016) 7887–7895.

[49] P. Wang, M. Chen, Towards power FPGA: architecture, modeling and control of multiport power converters, in: 2018 IEEE 19th Workshop on Control and Modeling for Power Electronics (COMPEL), 2018, pp. 1–8.

[50] S. Bandyopadhyay, P. Purgat, Z. Qin, P. Bauer, A multiactive bridge converter with inherently decoupled power flows, IEEE Trans. Power Electron. 36 (2) (February 2021) 2231–2245.

[51] P. Wang, Y. Chen, J. Yuan, R.C.N. Pilawa-Podgurski, M. Chen, Differential power processing for ultra-efficient data storage, IEEE Trans. Power Electron. 36 (4) (April 2021) 4269–4286.

[52] Y. Chen, P. Wang, Y. Elasser, M. Chen, Multicell reconfigurable multi-input multi-output energy router architecture, IEEE Trans. Power Electron. 35 (12) (December 2020) 13210–13224.

[53] L.F. Costa, G. Buticchi, M. Liserre, Quadruple active bridge dc–dc converter as the basic cell of a modular smart transformer, in: 2016 IEEE Applied Power Electronics Conference and Exposition (APEC), March 2016, pp. 2449–2456.

[54] J. Hiltunen, V. Väisänen, R. Juntunen, P. Silventoinen, Variable-frequency phase shift modulation of a dual active bridge converter, IEEE Trans. Power Electron. 30 (12) (December 2015) 7138–7148.

[55] M.N. Kheraluwala, R.W. Gascoigne, D.M. Divan, E.D. Baumann, Performance characterization of a high-power dual active bridge DC-to-DC converter, IEEE Trans. Ind. Appl. 28 (6) (November/December 1992) 1294–1301.

[56] J. Riedel, D.G. Holmes, B. McGrath, C. Teixeira, Maintaining continuous ZVS operation of a dual active bridge by reduced coupling transformers, IEEE Trans. Ind. Electron. 65 (12) (December 2018) 9438–9448.

[57] J. Lu, G. Liu, H. Bai, A. Brown, P.M. Johnson, M. McAmmond, A.R. Taylor, Applying variable-switching-frequency variable-phase-shift control and E-mode GaN HEMTs to an indirect matrix converter-based EV battery charger, IEEE Trans. Transp. Electrif. 3 (3) (September 2017) 554–564.

[58] R.W. Erickson, D. Maksimovi, Section 7.2: the basic AC modeling approach, in: Fundamentals of Power Electronics, second ed., Springer-Verlag, New York, 2001.

[59] L. Chen, L. Lin, S. Shao, F. Gao, Z. Wang, P.W. Wheeler, T. Dragicevic, Moving discretized control set model-predictive control for dual-active bridge with the triple-phase shift, IEEE Trans. Power Electron. 35 (8) (Aug. 2020) 8624–8637.